Optimal Apodization Design for Medical Ultrasound Using Constrained Least Squares Part II: Simulation Results

Drake A. Guenther and William F. Walker, *Member, IEEE*

***Abstract*—In the first part of this work, we introduced a novel general ultrasound apodization design method using constrained least squares (CLS). The technique allows for the design of system spatial impulse responses with narrow mainlobes and low sidelobes. In the linear constrained least squares (LCLS) formulation, the energy of the point spread function (PSF) outside a certain mainlobe boundary was minimized while maintaining a peak gain at the focus. In the quadratic constrained least squares (QCLS) formulation, the energy of the PSF outside a certain boundary was minimized, and the energy of the PSF inside the boundary was held constant. In this paper, we present simulation results that demonstrate the application of the CLS methods to obtain optimal system responses. We investigate the stability of the CLS apodization design methods with respect to errors in the assumed wave propagation speed. We also present simulation results that implement the CLS design techniques to improve cystic resolution. According to novel performance metrics, our apodization profiles improve cystic resolution by 3 dB to 10 dB over conventional apodizations such as the flat, Hamming, and Nuttall windows. We also show results using the CLS techniques to improve conventional depth of field (DOF).**

I. Introduction

In an accompanying paper [1], we describe two apodization design methods using a constrained least squares (CLS) formulation. The algorithms allow for the synthesis of beam patterns with a specified mainlobe width and minimum energy in the sidelobe regions. The CLS techniques express the system spatial impulse response (PSF) using a linear algebra formulation of the aperture weights and a propagation function. The propagation matrix uses superposition to describe the contribution of each transducer element at each field point at an instant in time and can be determined from experiment, simulation, or theory. The CLS formulations provide closed form solutions for the aperture weightings that minimize the energy of the PSF outside some specified boundary subject to either a linear or quadratic constraint on the weights. A brief review of the major results derived in [1] is provided below.

Manuscript received June 5, 2006; accepted November 1, 2006.

This work was supported by US Army Congressionally Directed Research Program Grant No. W81XWH-04-1-0590.

The authors are with the University of Virginia, Department of Biomedical Engineering, Charlottesville, VA (e-mail: dag2m@virginia.edu).

Digital Object Identifier 10.1109/TUFFC.2007.248

A. Linear Algebra Formulation of the Broadband Spatial Impulse Response

The sensitivity field for a transducer during pulse-echo imaging can be expressed as the product of a propagation matrix, S, and a set of aperture weightings, w. S can be derived from the Rayleigh-Sommerfeld diffraction equation, outlined in [2] and may include a term relating to limited element angular response [3] and frequency-dependent attenuation. The propagation matrix also can be simulated or measured experimentally. For our formulation, S is a function of the transmit aperture weights, the excitation pulse, and the individual element spatial impulse responses of the transmit and receive apertures. The two-way PSF, P, is then simply the matrix multiplication between the propagation matrix and the weight vector:

$$P = Sw. \tag{1}$$

B. Linearly Constrained Least Squares Apodization Design

In the first CLS apodization design technique, we minimize the energy of the PSF outside a certain mainlobe region subject to a linear constraint on the aperture weights. Although our formulation can account for the four-dimensional (4-D) nature of the spatiotemporal PSF, we restrict our analysis to two spatial dimensions, azimuth and range, and a single instant in time. The mainlobe region is defined by a circle of a specified radius centered at the peak of the 2-D PSF. Drawing upon [4], we can derive the least squares solution for the receive aperture weightings that produce the desired PSF:

$$w_{\text{opt}} = \left(S^T S\right)^{-1} C \left[C^T \left(S^T S\right)^{-1} C\right]^{-1}, \tag{2}$$

where the superscripts T and -1 denote the transpose and matrix inverse operations, respectively. S represents the propagation matrix for every spatial point of the PSF in which energy is to be minimized, and C is the linear constraint vector. The linear constraint, $C^T w = 1$, maintains a peak gain of the PSF at the intended focus. C has elements corresponding to the individual amplitude response of each synthetic receive element at the intended focus.

C. Quadratically Constrained Least Squares Apodization Design

The second CLS apodization design technique minimizes the energy of the PSF outside the defined mainlobe

region, while maintaining constant energy of the PSF inside the mainlobe region. We formulate this problem as a least squares minimization subject to a quadratic constraint on the weights. This method requires the formation of two propagation matrices. The first, S_{out}, represents the propagation matrix associated with every point of the PSF in which energy is to be minimized, as in (2). The second, S_{in}, represents the propagation matrix associated with every point of the PSF lying inside the mainlobe boundary and appears in the quadratic constraint, $\|S_{\text{in}}w\|^2 = 1$, where $\| \bullet \|^2$ denotes the square of the ℓ^2-norm. Drawing upon [5] and [6], the set of optimal receive weightings for this scenario is given by the generalized eigenvector corresponding to the minimum generalized eigenvalue resulting from the generalized eigenvalue decomposition problem of $S_{\text{out}}^T S_{\text{out}}$ and $S_{\text{in}}^T S_{\text{in}}$:

$$S_{\text{out}}^T S_{\text{out}} w = \lambda S_{\text{in}}^T S_{\text{in}} w, \tag{3}$$

where the weight vector w is the generalized eigenvector and λ is the associated generalized eigenvalue.

D. Reduced Computational Cost Through Symmetry Relations

The CLS apodization design techniques can become computationally expensive rather easily due to the large propagation matrices and the computation of the matrix inverse (only for the linear constrained least squares (LCLS) design case). In order to reduce this computational complexity, we exploit the lateral symmetry of the aperture and the PSFs that arise from symmetric, nonsteered apertures [1]. Due to the symmetry relationships, we need only compute half of the aperture weights using just half of the PSF, thereby enabling more efficient computation of the apodization profiles. Note that, although the design and calculation of the weights is computationally costly, the application of the weights is trivial in modern ultrasound system hardware. Once the CLS apodization profiles have been calculated, they can be stored in a lookup table and applied as dynamic apodization with range.

All the formulas for the design methods described above are thoroughly described and derived in [1]. This paper presents results of simulations that were implemented to demonstrate the validity and stability of the LCLS and quadratic constrained least squares (QCLS) apodization design techniques.

II. Simulations

In order to test our apodization design algorithms and to highlight the utility of the cystic resolution metric [8] we performed simulations using DELFI [7], a custom ultrasound simulation tool that efficiently computes spatial pulse-echo responses. All simulations were performed under MATLAB (The Mathworks, Inc., Natick, MA). Spatial pulse-echo responses were computed by transmitting a focused wave from a fixed f/# aperture and synthetically receiving on each individual element in the array. Uniform apodization was applied on transmit. Dynamic receive focusing was used to calculate multiple PSFs at varying depths. The focal ranges on receive were 1 cm, 1.5 cm, 2 cm, 2.5 cm, and 3 cm. The PSFs were computed at the instant in time corresponding to the given receive depth and over a 2-D planar area in azimuth and range that encompassed the entire extent of the PSF.

TABLE I
Parameters Used in General CLS Apodization Design and Speed of Sound Simulations.

Parameter	Value
Number of elements	192
Element pitch	200 μm
Focus	2.0 cm
PSF window lateral sampling interval	34 μm
PSF window axial sampling interval	20 μm
Ultrasonic wave propagation speed	1545 m/s
Frequency	6.5 MHz
Fractional bandwidth	50%

TABLE II
Parameters Used in General CLS Apodization Design and F/# Simulations.

Parameter	Value
Number of elements	192
Element pitch	150 μm
Focus	2.0 cm
PSF window lateral sampling interval	25 μm
PSF window axial sampling interval	20 μm
Ultrasonic wave propagation speed	1545 m/s
Frequency	10 MHz
Fractional bandwidth	75%

We simulated two different 1-D linear arrays. The first array, whose system parameters are described in Table I, operated at 6.5 MHz center frequency with a 50% fractional bandwidth calculated as:

$$\text{Fractional BW}\,(\%) = \frac{\text{BW}}{f_c} \times 100, \tag{4}$$

where f_c is the center frequency of the transmitted pulse in megahertz and BW is the -6 dB bandwidth of the pulse also in megahertz. The array had fixed transmit focus at 2 cm (f/2). The 6.5 MHz array was used for general CLS apodization design and for the speed of sound simulations. The second array was more aggressive with a higher operating frequency of 10 MHz with a 75% fractional bandwidth. We kept the transmit focus fixed at 2 cm but used a larger f/# on transmit (f/4). This array also was used for apodization design and for the varying receive f/# simulations. The system parameters for the second array are described in Table II.

Constrained least squares apodization profiles were designed and analyzed for improvements in system perfor-

mance relative to conventional apodization. All calculations were performed on an IBM Intellistation Z Pro (Processor speed 2.80 GHz, 3.00 Gb RAM, IBM Corporation, Armonk, NY). In general the CLS apodization profiles took less than two minutes of CPU time to generate, and the QCLS profiles were faster to generate than the LCLS profiles because they do not require computing a matrix inverse. The 2-D PSFs generated using DELFI [7] were used to calculate the optimal receive weights according to the CLS algorithms outlined above. CLS apodization profiles were computed for each dynamic receive response because of the spatial shift variance of the PSF with range. The sidelobe region was defined by centering a cyst of a specified radius about the mainlobe peak of the PSF. As this cyst specifies the mainlobe and sidelobe regions of the PSF, we call it the "design cyst." Cystic contrast, neglecting electronic signal-to-noise ratio (SNR), was computed according to the equation given in [8] as:

$$C = \sqrt{\frac{E_{\text{out}}}{E_{\text{tot}}}}, \tag{5}$$

where E_{out} is the energy of the PSF outside the mainlobe boundary, and E_{tot} is the entire energy of the PSF. Note that the best achievable contrast occurs when the cyst void encompasses the entire PSF. In this scenario, C in (5) would be 0. Therefore, when quantifying cystic contrast, a C value closer to 0, or more negative on a decibel scale, indicates better performance. Corresponding cystic contrast curves as a function of cyst radius were calculated for the CLS windows and compared to those for the flat, Hamming, and the Nuttall [21] windows.

To investigate the performance of the algorithms, we computed apodization profiles for a large number of design cyst radii. Specifically, we present results of LCLS and QCLS aperture weights with design cyst radii from 0.1 mm to 2.0 mm. We also computed the weights that minimized the mainlobe width for the LCLS design case in order to test the limits of this particular algorithm.

Because most commercial systems use dynamic receive focusing to improve image contrast and extend the conventional DOF, we investigated the stability of our algorithms in this scenario. We calculated PSFs at varying depths on receive (1.0 cm, 1.5 cm, 2.0 cm (Tx focus), 2.5 cm, and 3.0 cm) then applied the CLS algorithms on each PSF. The resulting aperture weights should improve DOF because the goal of applying the CLS algorithms was to make PSFs with a similar mainlobe and minimum sidelobe energy.

An important system parameter that affects image quality and contrast is the f/# used on receive. It is an important parameter for a linear array because dynamic focusing schemes that maintain constant f/# throughout the image range are limited by aperture size. We investigated the impact of f/# on our CLS apodization design algorithms by computing contrast curves as a function of cyst radius for varying f/#'s.

Errors in the assumed sound wave propagation velocity adversely affect an ultrasound system's response, potentially degrading the resulting images [9]. Because our CLS technique uses dynamic shift variant aperture weights, errors in the assumed sound speed are of great concern. Therefore, we implemented simulations in which the assumed propagation speed was underestimated by 1%, 3%, and 5%, and overestimated by 1%, 3%, and 5%. The PSFs were calculated at the instant in time corresponding to the intended transmit focus of 2 cm assuming 1545 m/s. Due to different propagation speeds through the medium, however, the PSFs shifted in range. The purpose of these simulations was to investigate the robustness of our algorithm to incorrect assumptions about the wave propagation speed.

III. Results

Optimal receive apodization profiles were computed for a linear 1-D array according to the CLS formulations discussed above. Cystic resolution curves were calculated in order to visualize and quantify the changes in system performance using the CLS windows compared to the conventional windows. Apodization profiles were computed for a range of design cyst radii from 0.1 mm to 2.0 mm. For every design cyst radius, the CLS apodization profiles resulted in PSFs that had lower energy in the sidelobe regions compared to the other windows.

Fig. 1 shows results for the 6.5 MHz simulations with a fixed transmit focus at 2 cm (f/2) and dynamic receive focus at 2 cm (f/1). The plot on the left shows an up close view of the mainlobe region of the integrated lateral beamplots using different apodization schemes. All lateral beamplots were computed by taking the square root of the energy of the 2-D PSF summed in range. The CLS profiles were designed using a cyst radius of 0.6 mm. We also used the LCLS algorithm to design an apodization profile that produces a PSF with the narrowest possible mainlobe. This beamplot is the mCLS plot in Fig. 1 designated by a □ marker. The full width at half maximums (FWHM), −6 dB beamwidths, were 264, 304, 328, 297, 301, and 190 μm for the flat, Hamming, Nuttall, LCLS, QCLS, and mCLS apodizations, respectively. The LCLS and QCLS apodization profiles had smaller −6 dB beamwidths than all but one of the conventional windows. The LCLS and QCLS lateral beamplots have decreased sidelobe levels by about 5 dB relative to the Hamming window, 12 dB below the flat apodization, and almost 16 dB below the Nuttall window. The mCLS apodization lateral beamplot has the narrowest mainlobe (20% reduction compared to the flat window) but the highest sidelobe levels. The plot on the right shows the full extent of the integrated lateral beamplots of the PSFs with notable differences in the grating lobe levels. The reduction of the sidelobe levels for the LCLS and QCLS apodization profiles did result in higher grating lobes than the Hamming and Nuttall windows, but these larger grating lobes are around −60 dB, a typical noise floor for diagnostic ultrasound imaging systems [10]. The mCLS lateral beamplot shows much larger grating lobes around −40 dB.

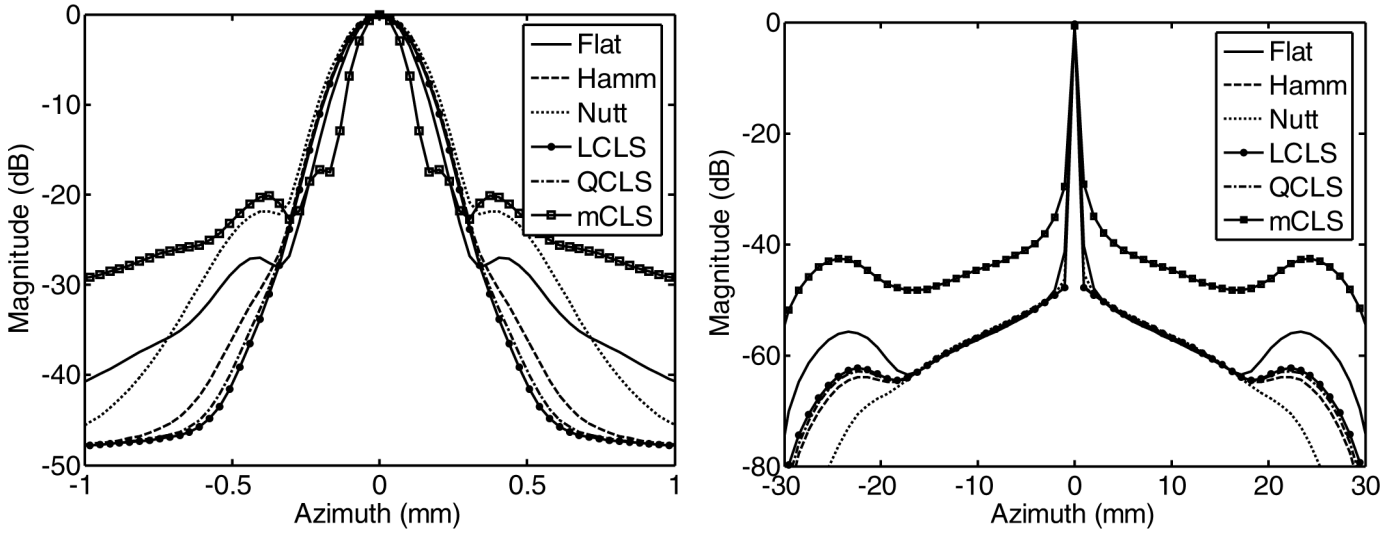

Fig. 1. Integrated lateral beamplots for different apodization schemes with the 1-D linear array operating at 6.5 MHz center frequency, fixed Tx focus at 2 cm (f/2) and dynamically focused on Rx at 2 cm (f/1). The LCLS and QCLS profiles were designed with a cyst radius of 0.6 mm. Note that the LCLS and QCLS profiles yield sidelobe levels lower than and mainlobe widths comparable to all other apodizations.

A. Effects of the Design Cyst Radius on the CLS Apodization Algorithms

Because it is unreasonable to scan through apodization profiles for every cyst radius with conventional systems, it is interesting to monitor the behavior of the CLS apodization profiles with increasing design cyst radius. Furthermore, using contrast curves we can easily compare the performance of the different apodization schemes and optimize based on required operation values. In Fig. 2 we show the performance of both the LCLS apodization windows (left column) and the QCLS apodization windows (right column) as we increase the design cyst radius from 0.2 mm to 0.8 mm in 0.2 mm steps. These simulations used the 6.5 MHz linear array conditions described in Table I. The results at different dynamic receive depths were similar so we present one set of simulation results in Fig. 2 corresponding to a dynamic receive depth of 1.5 cm. The first row of plots, panels (a) and (b), shows the contrast curves over cyst radii from 0.1 mm to 1.0 mm. For the LCLS windows, (a), we see a general trend of decreased contrast for the smaller cyst sizes when increasing the design cyst radius. At the same time, we see greatly improved contrast over a large range of cyst radii for the larger design radius curves. Overall the LCLS windows maintained relatively similar contrast curves for design cyst radii of 0.4, 0.6, and 0.8 mm. These profiles improved contrast around 5 dB relative to the flat apodization scheme across the range of larger cyst sizes (0.4 mm–1.0 mm). The QCLS contrast curves changed more than the LCLS curves across the range of design cyst radii. Each QCLS apodization profile achieved the best contrast of any window for the specific design radius; however, the QCLS profiles suffered greater losses in contrast for cyst sizes smaller than the design cyst radius compared to the LCLS profiles designed for the same cyst radius. This phenomenon can be seen easily with the 0.6 mm and 0.8 mm contrast curves where they decrease contrast by about 3 dB compared to the flat apodization for cyst radii smaller than 0.4 mm. The second row of plots in Fig. 2 shows the mainlobe region of the CLS integrated lateral beamplots. The widening of the mainlobe for the QCLS profiles is more dramatic than the LCLS profiles. This phenomenon is to be expected due to the formulation of the QCLS algorithm, which minimizes the ratio of PSF energy outside the cyst to PSF energy inside the cyst. The third row of plots, panels (e) and (f), shows the changes in the grating lobes with different design cyst radius.

The final row of plots in Fig. 2 shows the designed apodization weights for each individual element. For the most part, the CLS profiles have a typical smooth, curved shape like many of the conventional windows; however, the CLS windows' behavior at the ends of the aperture is discontinuous. These apodization profiles also show that some outer elements have negative weights and large magnitudes, a phenomenon never seen in the conventional window functions. The positive-negative discontinuity at the edges of the aperture is indeed an intriguing result. The outer elements in an aperture contribute high lateral spatial frequency content, which can sharpen the mainlobe of the overall response [11]. However, these elements also give the PSF "wings," clouds of energy outside the mainlobe region that spread in azimuth and range. Conventional apodization functions typically suppress the outer elements of an aperture to decrease this sidelobe energy. However, this reduces the high lateral spatial frequency content in the overall response. It appears that the positive-negative discontinuity at the edges of the CLS apodization functions is a novel way to sharpen the PSF's mainlobe and reduce the energy in the PSF's "wings" through destructive interference.

In the simulations that used the 10 MHz array configuration, we calculated CLS apodization profiles for a number of different cyst radii. Through this investigation we

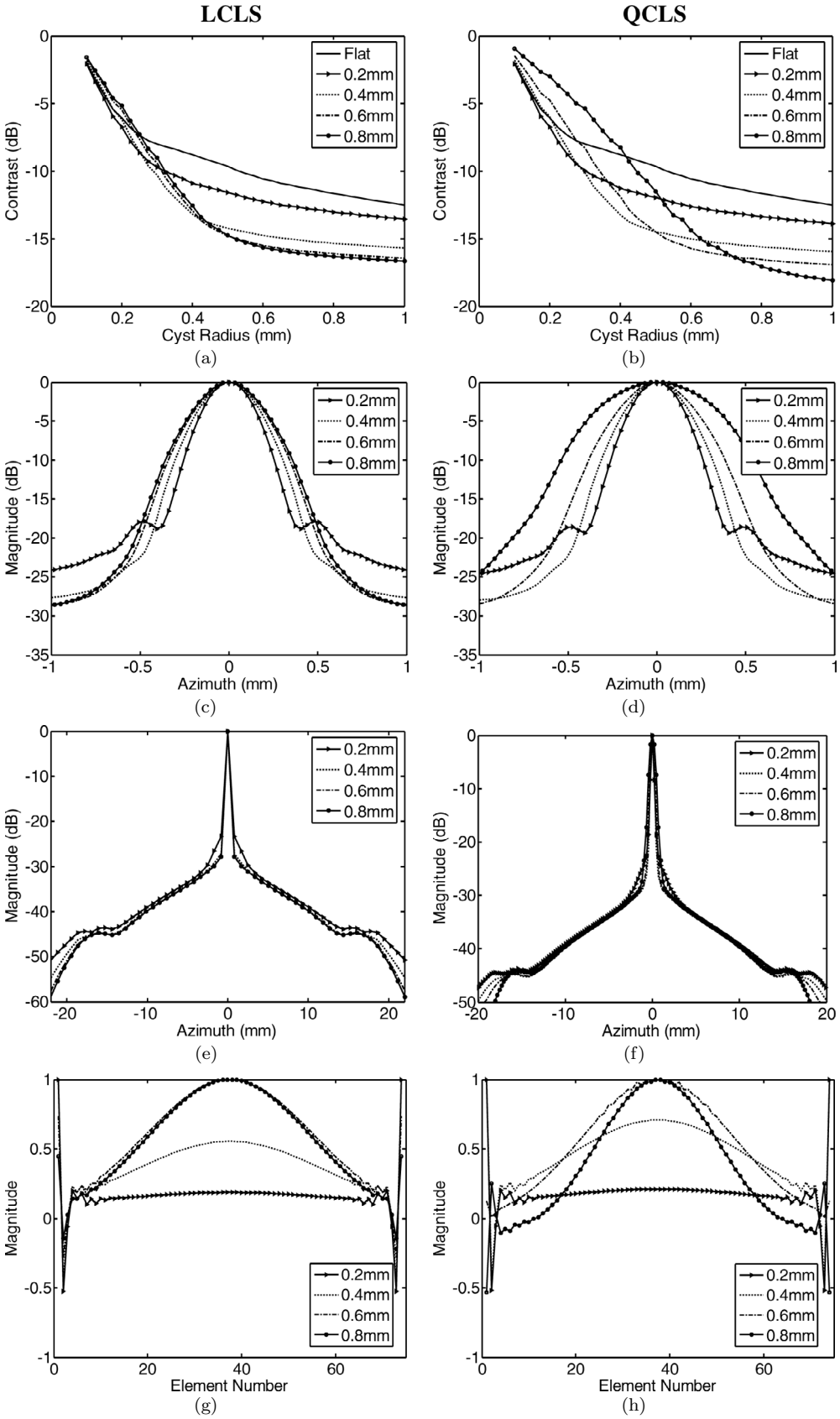

Fig. 2. Comparison of CLS apodization given different design cyst radii. The entire left column corresponds to the LCLS algorithm, and the right column corresponds to the QCLS algorithm. (a) and (b) show the associated contrast curves over a range of cyst sizes compared to the flat apodization profile. Panels (c) and (d) show the mainlobe behavior of the CLS windows. The third row, panels (e) and (f), gives the full range of the integrated lateral beamplots. (g) and (h) plot the apodization profile versus element number. Note how the mainlobe width trends with increasing design radius are indicative of the contrast performance between the two algorithms.

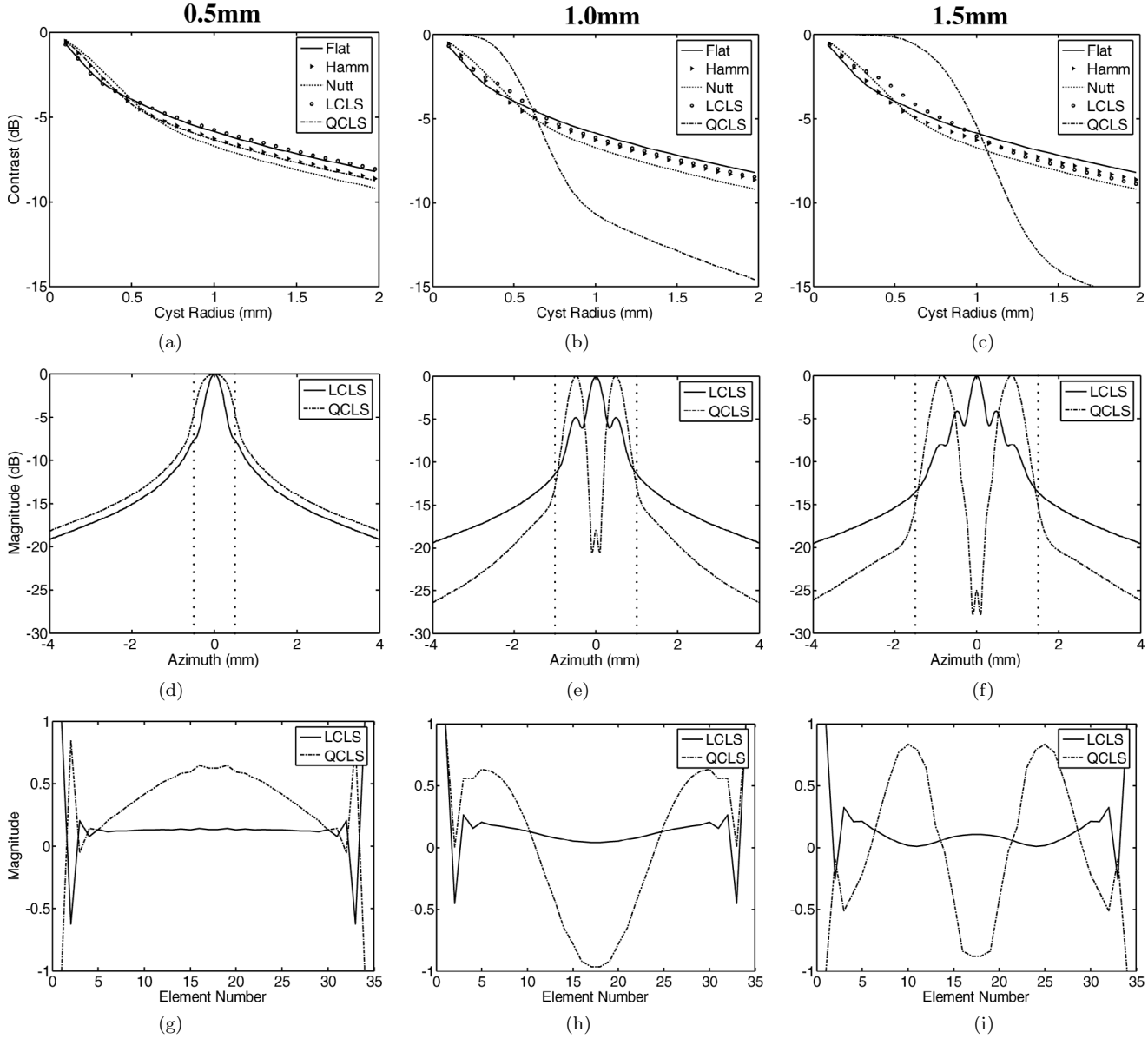

Fig. 3. Comparison of apodization profiles with large design cyst radius. Panels (a)–(c) plot the contrast curves for design radii of 0.5 mm, 1.0 mm, and 1.5 mm, respectively. The second row of plots shows the integrated lateral beamplots. The third row of plots, panels (g)–(i), shows the LCLS and QCLS apodization profiles as a function of element number across the aperture. Note that, for larger design radii, the QCLS algorithm results in PSFs with multiple peaks in the mainlobe region.

observed a peculiar phenomenon for the QCLS algorithm for the larger design cyst radii. Because the algorithm attempts to keep the energy of the PSF inside the cyst boundary constant, when larger design cyst radii are used, the QCLS weights make a PSF with multiple peaks. This is equivalent to the eigenfilter design approach in which the frequency response ripples in the pass band [12], [13]. Fig. 3 plots (e) and (f) accurately depict this phenomenon. These data use the 10 MHz array described in Table II with a dynamic receive focus at 1.0 cm (f/2). The first row of plots in Fig. 3(a)–(c), shows the contrast curves for increasing design radii of 0.5 mm, 1.0 mm, and 1.5 mm, respectively. Note for the larger design radii, the QCLS algorithm results in contrast improvements ranging from 5 dB to 10 dB but poor contrast resolution for smaller cyst sizes. Fig. 3 plots (d)–(f) show the integrated beamplots for the LCLS and QCLS apodization profiles. Here we see how the QCLS algorithm was able to achieve the dramatic contrast improvements for the larger cyst sizes by having multiple mainlobes inside the cyst boundary. Likewise, for large design radii, the LCLS apodization profile results in higher sidelobes inside the boundary in order to achieve lower sidelobes outside the boundary.

The modulation of the mainlobe in the QCLS PSFs would not be an ideal spatial response for general imaging purposes. Notice that the shape of the QCLS apodization profiles that yield multiple mainlobe peaks are approximately sinusoidal [Fig. 3 panels (h) and (i)]. According to the Fraunhoffer approximation, which states that the spatial response of an aperture is the Fourier transform

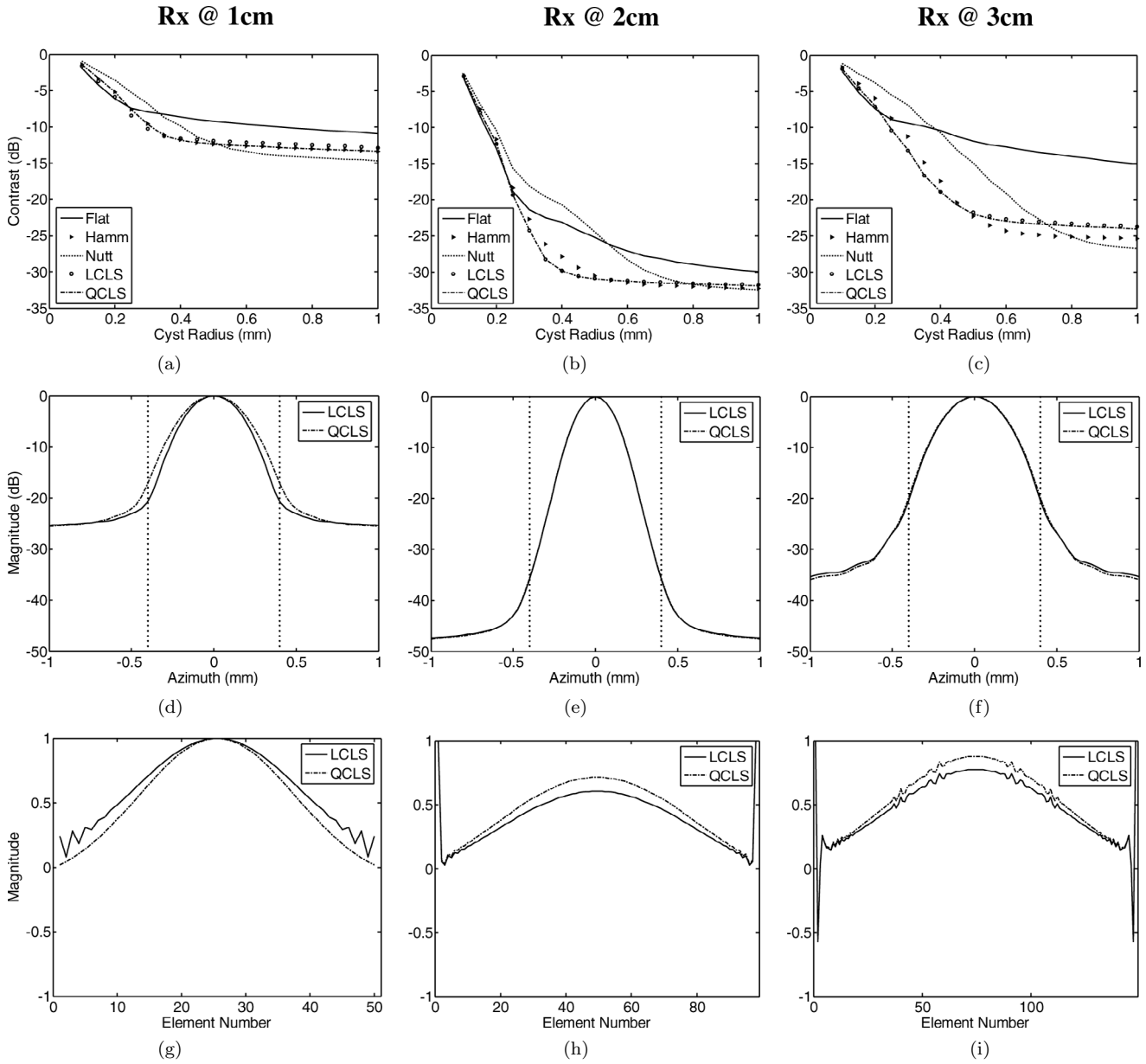

Fig. 4. Comparison of apodization profiles at different dynamic receive foci of 1 cm, 2 cm, and 3 cm and constant f/# (f/1). Panels (a)–(c) show contrast curves for the different apodization schemes (flat, Hamming, Nuttall, LCLS, and QCLS). The second row of plots, (d)–(f), show the integrated beamplots of the CLS profiles in which the dotted line corresponds to the cyst boundary used to design the windows. Plots (g)–(i) show the magnitude of the CLS profiles across the aperture. The CLS profiles improve contrast over a range of smaller cysts at all dynamic receive focal depths.

of the aperture function [2], a rectangular windowed sinusoidal aperture function should result in a lateral spatial response resembling two sinc functions (the convolution between a sinc and two impulses). These two sinc functions correspond to the two mainlobes in the responses seen in Fig. 3 panels (e) and (f). Furthermore, note that, when the frequency of the sinusoid corresponding to the aperture definition is increased [comparing panel (h) to panel (i)], the two mainlobes of the spatial response separate further in azimuth [panel (e) and (f)]. This result is consistent with Fourier transform theory.

Clearly imaging with a PSF that has two mainlobes should not produce an image of a cyst with 10 dB contrast improvement, as the contrast curves of Fig. 3 panels (b) and (c) suggest. However, there are applications in which lateral modulation of the PSF could prove beneficial [14], [15]. For example, such a PSF could be used in Doppler ultrasound for which acquiring the axial as well as lateral component of velocity can lead to more accurate estimation of the velocity vector [16]. Other applications could include designing ultrasound spatial responses for hyperthermia treatments during which control over localized energy delivery is paramount [17]. We also are investigating ways to modify the QCLS apodization design formulation to reduce the modulation/multiple peak effect to an equiripple, similar to finite impulse response (FIR) filter design [18]. One possible method is to use the weighting function discussed and derived in [1]. Applying a weighting function to

the mainlobe region of the PSF that emphasizes the focal point compared to the surrounding area would yield a PSF with a single mainlobe. Preliminary results show that the weighting can be applied to the QCLS algorithm to mitigate the multiple mainlobe effect. The resulting QCLS weights produce PSFs whose lateral beamplots are similar to the LCLS beamplots in Fig. 3 panels (e) and (f) with slightly higher sidelobes inside the cyst boundary.

B. Effects of Dynamic Receive Focusing on the CLS Apodization Algorithms

In our simulations, we also investigated the effects of dynamic receive focusing on the performance of the CLS algorithms. Conventional systems typically maintain a constant beamwidth over a large range by transmitting on a higher f/# and dynamically receiving with a constant, lower f/#. Because our apodization design schemes effectively control mainlobe size, we expect to see improvements in DOF. For these simulations, we used the 6.5 MHz linear array setup with the fixed transmit focus at 2 cm (f/2), then we dynamically received focused data at 1 cm, 1.5 cm, 2 cm, 2.5 cm, and 3 cm with an f/1 aperture. CLS apodization profiles were designed with an aggressive cyst radius of 0.4 mm for the PSFs at each range. Fig. 4 shows the results from these dynamic receive focused and apodized simulations. We show only data from dynamic receive depths of 1 cm, 2 cm, and 3 cm because the data at the other two depths showed similar trends. Fig. 4 panels (a)–(c) show the contrast curves for the different apodization schemes across cyst radii. The LCLS and QCLS contrast curves for all three ranges are very similar, hence why the QCLS curve is difficult to distinguish. The reduced contrast at the 1 cm and 3 cm depths can be attributed to the spreading of the mainlobe away from the transmit focus. At all three ranges, the CLS apodization schemes show marked contrast improvements over the flat and Nuttall apodization schemes across a large range of cyst sizes and reasonable improvements over the Hamming window at smaller cyst radii. Both the Hamming and the Nuttall window outperform the CLS apodization profiles for cyst radii greater than 0.5 mm when receiving at 1 cm, but these improvements are a modest gain of about 2 dB. Panels (d)–(f) of Fig. 4 show the mainlobe characteristics of integrated lateral beamplots using the CLS apodization profiles. The dotted vertical lines on these images correspond to the cyst boundary used to design the windows. Mainlobes for the LCLS and QCLS windows are quite similar for the three different ranges. The third row of plots in Fig. 3 shows the designed apodization weights for the LCLS and QCLS profiles across the aperture. Note that the aperture size increases with range to maintain a constant f/# on receive. These profiles show discontinuities of the weighting function at the edges of the aperture.

In order to investigate the improvements in DOF for the CLS algorithms compared to the conventional windows, we looked at the beamwidths of the integrated beamplots at −6 dB (FWHM) and −20 dB. We also show images of the

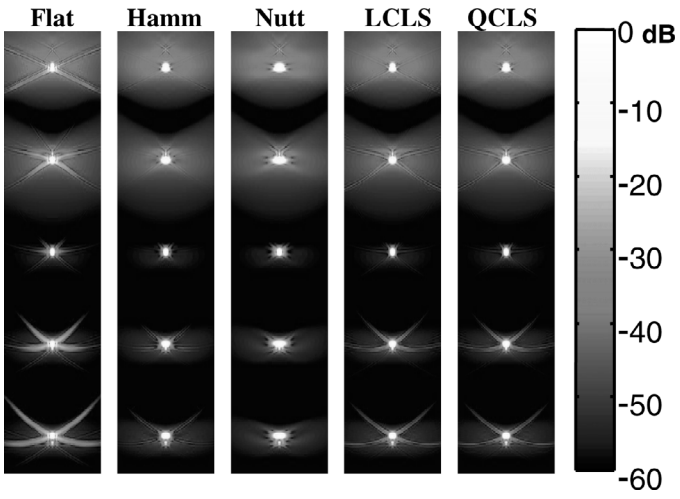

Fig. 5. Comparison of 2-D PSFs of different apodization profiles with range on dynamic receive. The CLS profiles were designed using a cyst radius of 0.4 mm. The system had a transmit focus at 2 cm (f/2), then was dynamically focused and apodized at ranges of 1 cm, 1.5 cm, 2 cm, 2.5 cm, and 3 cm (f/1). Each image was normalized and log compressed to −60 dB. Note the spreading of the mainlobe in the conventional windows PSFs away from the transmit focus and the relatively constant mainlobe of the CLS apodized PSFs.

2-D PSFs for the 6.5 MHz array at each range superimposed to qualitatively depict the constant mainlobe size with range. In Fig. 5 we show images of the 2-D PSFs at each range for flat, Hamming, Nuttall, LCLS, and QCLS apodization profiles. The CLS profiles were designed using a cyst radius of 0.4 mm. The images are 1 cm in azimuth and extend from 0.8 cm to 3.2 cm in range. Each image was normalized and log compressed to −60 dB. The CLS apodization profiles maintain a relatively constant mainlobe size through range compared to the mainlobe spreading seen in the Hamming and Nuttall windows. The sidelobes of the CLS profiles are higher than the Hamming and Nuttall windows at the 2.5 and 3 cm depths but lower than the large sidelobes evident in the flat apodization PSFs. Fig. 6 plots the −6 dB (FWHM) and −20 dB beamwidths of the PSFs for the different apodizations at all five ranges. In Fig. 6 we see that the CLS apodization profiles maintain a relatively constant beamwidth with range compared with the Nuttall and Hamming windows. The flat apodization profile maintains a somewhat constant FWHM level across range but deviates greatly with range at the −20 dB level; whereas the CLS profiles remain relatively constant.

We also produced similar images for the CLS apodization profiles using a design cyst radius of 0.6 mm in Fig. 7. Again, the CLS apodization profiles maintain a relatively constant mainlobe size across ranges compared to the mainlobe spreading evident with the Hamming and Nuttall windows. The sidelobes of the CLS profiles are suppressed at the 2.5 and 3 cm depths compared to Fig. 5. The QCLS PSF exhibits a larger mainlobe with higher sidelobes at 1 cm dynamic receive, a phenomenon due to the algorithm maintaining constant energy of the PSF inside the cyst boundary. This effect is quantified in Fig. 8, in which the QCLS profile exhibits the largest FWHM

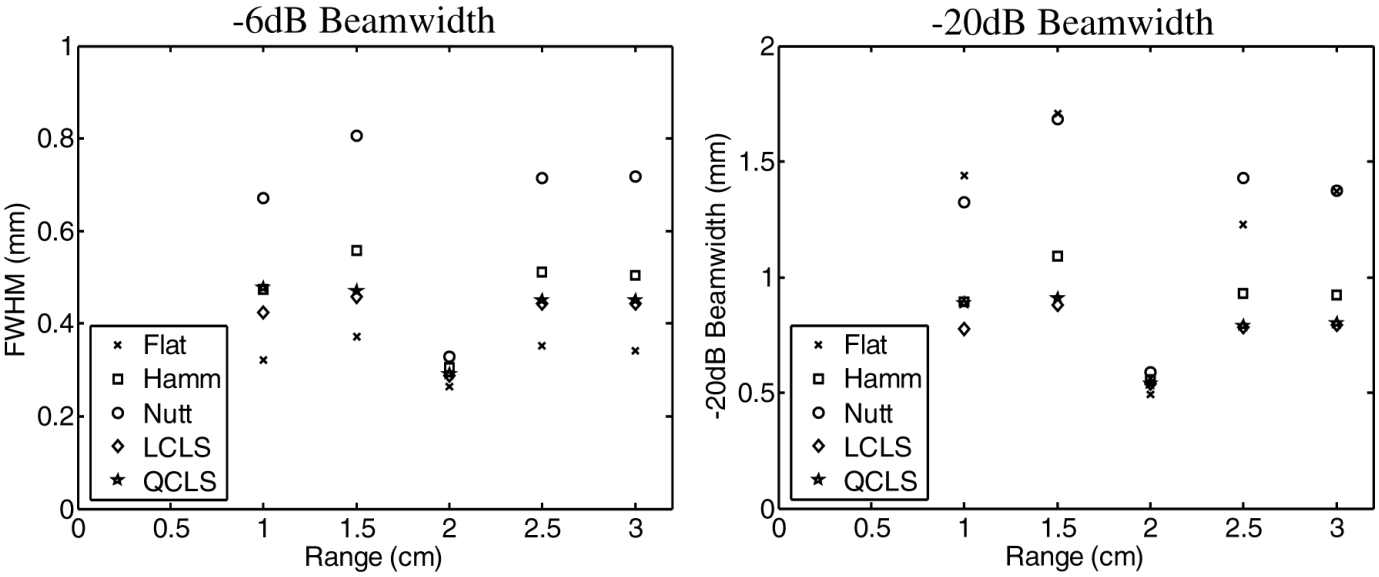

Fig. 6. Comparison of the −6 dB (FWHM) and −20 dB beamwidths of the PSFs for different apodization profiles with range on dynamic receive. The CLS apodization profiles were designed using a cyst radius of 0.4 mm. The system had a transmit focus at 2 cm (f/2), then was dynamically focused and apodized at ranges of 1 cm, 1.5 cm, 2 cm, 2.5 cm, and 3 cm (f/1). The FWHM and the −20 dB beamwidths of the CLS PSFs remain stable in range. They also achieve the narrowest −20 dB beamwidths away from the transmit focus.

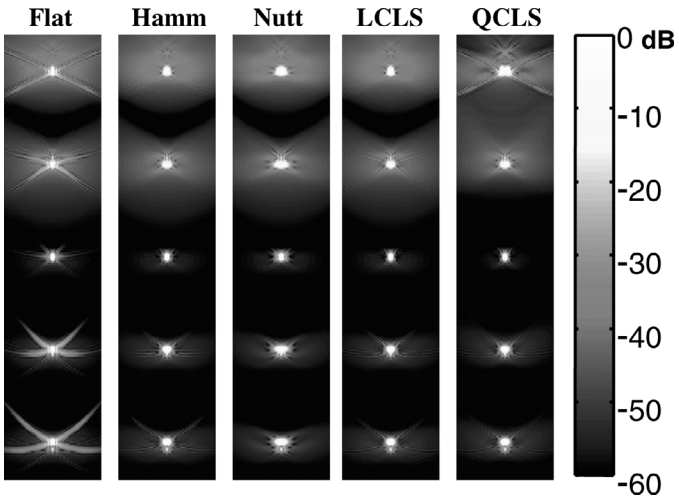

Fig. 7. Comparison of 2-D PSFs of different apodization profiles with range on dynamic receive. The CLS profiles were designed using a cyst radius of 0.6 mm. The system had a transmit focus at 2 cm (f/2), then was dynamically focused and apodized at ranges of 1 cm, 1.5 cm, 2 cm, 2.5 cm, and 3 cm (f/1). Each image was normalized and log compressed to −60 dB. Notice the greater sidelobe suppression of the CLS profiles in the deeper ranges compared to Fig. 5.

at a range of 1 cm. Other than this anomaly, the CLS apodization profiles exhibit a relatively constant FWHM and −20 dB beamwidth across range.

C. Effects of Receive F/# on the CLS Apodization Algorithms

The effect of f/# on receive was investigated to test the robustness of the CLS apodization design algorithms. For these simulations, we used the more aggressive 10 MHz array using a fixed transmit focus at 2 cm (f/4) and dynamic receive focusing and apodization. F/#'s ranging from f/0.5 to f/4 were used on receive, which varied the size of the receive aperture. Therefore, CLS apodization profiles were calculated for each receive aperture using a 0.6 mm design cyst radius. Fig. 9 shows the results of these simulations. The data show three different f/#'s used (f/0.5, f/2, and f/4) while dynamically receiving at 2.0 cm in range. We also analyzed the CLS algorithms at 1.0 cm and 3.0 cm in range, and they gave similar results. Panels (a)–(c) in Fig. 9 show the contrast curves for the different apodization profiles across a range of cyst radii. In general, contrast improves for all windows with smaller f/#'s. The CLS apodization profiles show modest contrast gains (1 dB to 3 dB) relative to the flat, Hamming, and Nuttall windows. The contrast improvements of the CLS windows over the conventional windows increase with increasing f/#. It is interesting to note that the Hamming and Nuttall windows have worse cystic resolution than the flat, LCLS, and QCLS windows at f/2 and f/4 across the entire range of cyst radii. This is a phenomenon we did not observe in the previous 6.5 MHz array simulations. The Hamming and Nuttall windows increase the size of the mainlobe in order to achieve sidelobe suppression. Furthermore, when analyzed with the cystic resolution metric, the decrease in sidelobe energy of the Hamming and Nuttall PSFs does not outweigh their relative increase in mainlobe width. The CLS apodization profiles, on the other hand, are able to maintain a narrow mainlobe width while decreasing the energy in the sidelobe region. Hence, improving cystic contrast. The second row of plots, (d)–(f), in Fig. 9 show the mainlobe region of the CLS integrated beamplots. The dotted line is the boundary of the design cyst radius of 0.6 mm. We see very little difference be-

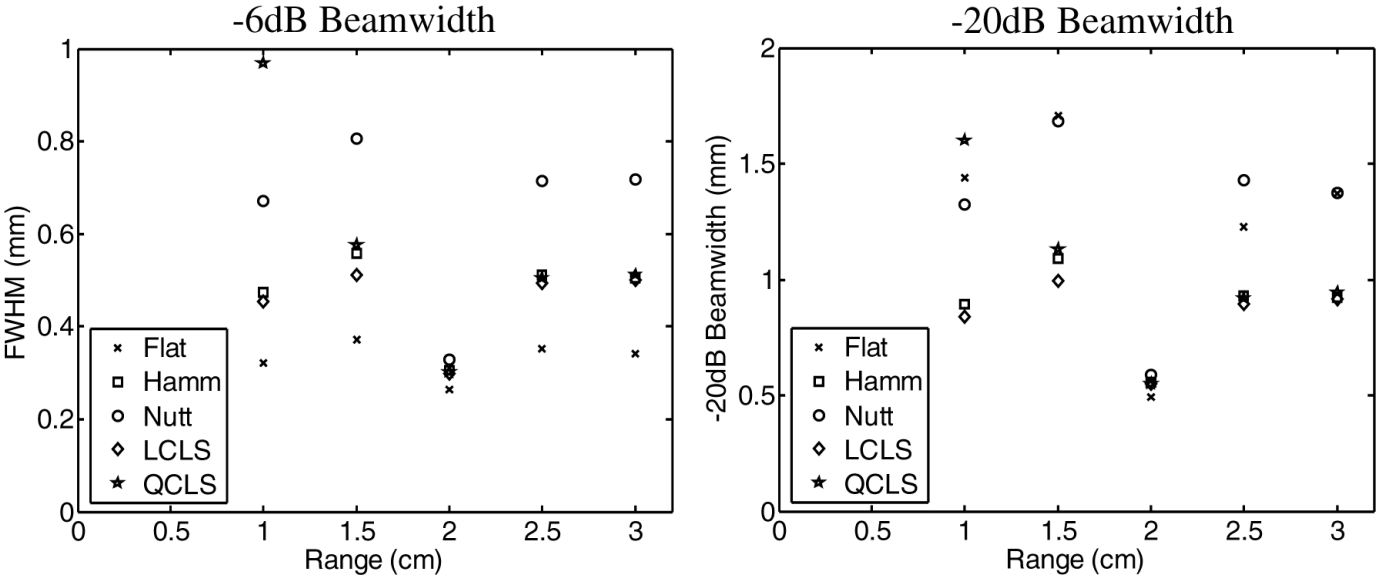

Fig. 8. Comparison of the −6 dB (FWHM) and −20 dB beamwidths of the PSFs for different apodization profiles with range on dynamic receive. The CLS apodization profiles were designed using a cyst radius of 0.6 mm. The system had a transmit focus at 2 cm (f/2), then was dynamically focused and apodized at ranges of 1 cm, 1.5 cm, 2 cm, 2.5 cm, and 3 cm (f/1). Notice the large FWHM of the QCLS algorithm compared to Fig. 6 at a range of 1 cm, a phenomenon due to the algorithm's attempt to maintain constant energy of the PSF inside the mainlobe region.

tween the two mainlobes, with the QCLS mainlobe a bit wider than the LCLS mainlobe. The third row of plots in Fig. 9 shows the weights of the CLS apodizations across the aperture. For the lower f/#'s, the difference between the CLS windows are greater.

Changing the f/# on receive did not produce results that we intuitively expected. We assumed that operating the CLS algorithms with smaller f/#'s or larger apertures would yield markedly better contrast curves than the conventional windows. Even though the CLS algorithms had more information to use in potentially achieving smaller sidelobe levels, the synthetic responses simply could not be summed together at that instant in time in order to destructively interfere. Ultimately, the algorithms still are governed by diffraction. Although large gains in contrast were not achieved with smaller f/#'s, the LCLS and QCLS profiles did achieve improved contrast (2 dB to 4 dB) compared to the conventional windows at the f/#'s investigated. Note that increasing the receive aperture size with range, a method typically used to maintain a constant f/# and improve DOF, is not entirely necessary with the CLS algorithms. It may be possible to use a fixed number of elements in the receive aperture at all ranges and let the algorithms control beam size. This is a method we are currently investigating.

D. Effects of Sound Speed Errors on the CLS Apodization Algorithms

In our final set of simulations, we investigated the sensitivity of the CLS apodization design algorithms to errors in the assumed speed of acoustic wave propagation. We performed these simulations using the 6.5 MHz array with a transmit focus at 2.0 cm (f/2) and a receive focus at 2.0 cm (f/1). For these simulations, the system always assumed a sound speed of 1545 m/s. Therefore, even when the propagation speed varied, the system never changed the transmit and receive focal delays. For all the simulations, the receive apodization applied was always the CLS apodization profile computed for the 1545 m/s PSF dynamically focused at 2.0 cm and with a design cyst radius of 0.6 mm. Fig. 10 shows the contrast curves (left) and integrated lateral beamplots (right) for the CLS apodizations with the correct sound speed in the medium of 1545 m/s. Fig. 10 should be used as a reference for the simulation results presented in Figs. 11 and 12. We obtained PSFs when the speed of sound was overestimated by 1%, 3%, and 5%, then underestimated by 1%, 3%, and 5%. Because the system always assumed a sound speed of 1545 m/s, the different propagation speeds shifted the PSFs in range. In order to be consistent when applying the cystic resolution metric, the cyst was shifted in range so that it was always centered on the degraded PSF. Fig. 11 shows the results for the simulations when the assumed speed of sound was overestimated, meaning that the true propagation speed through the medium was less than 1545 m/s. The first row of plots, (a)–(c), in Fig. 11 shows the contrast curves that were computed with the cyst centered on the shifted PSF. The Hamming, LCLS, and QCLS curves are similar for the 5%, 3%, and 1% overestimation. The Nuttall window interestingly achieves the best contrast at all cyst radii for the 5% overestimation simulation, but it is the worst in the 0.1–0.5 mm cyst radii range in the 1% overestimation. The second row of plots in Fig. 11 shows the mainlobe region of the integrated lateral beamplots for the CLS apodized PSFs. Panels (g)–(i) in Fig. 11 show the entire lateral extent of the integrated beamplots in which differences in the grating lobes for the CLS apodized PSFs can be seen.

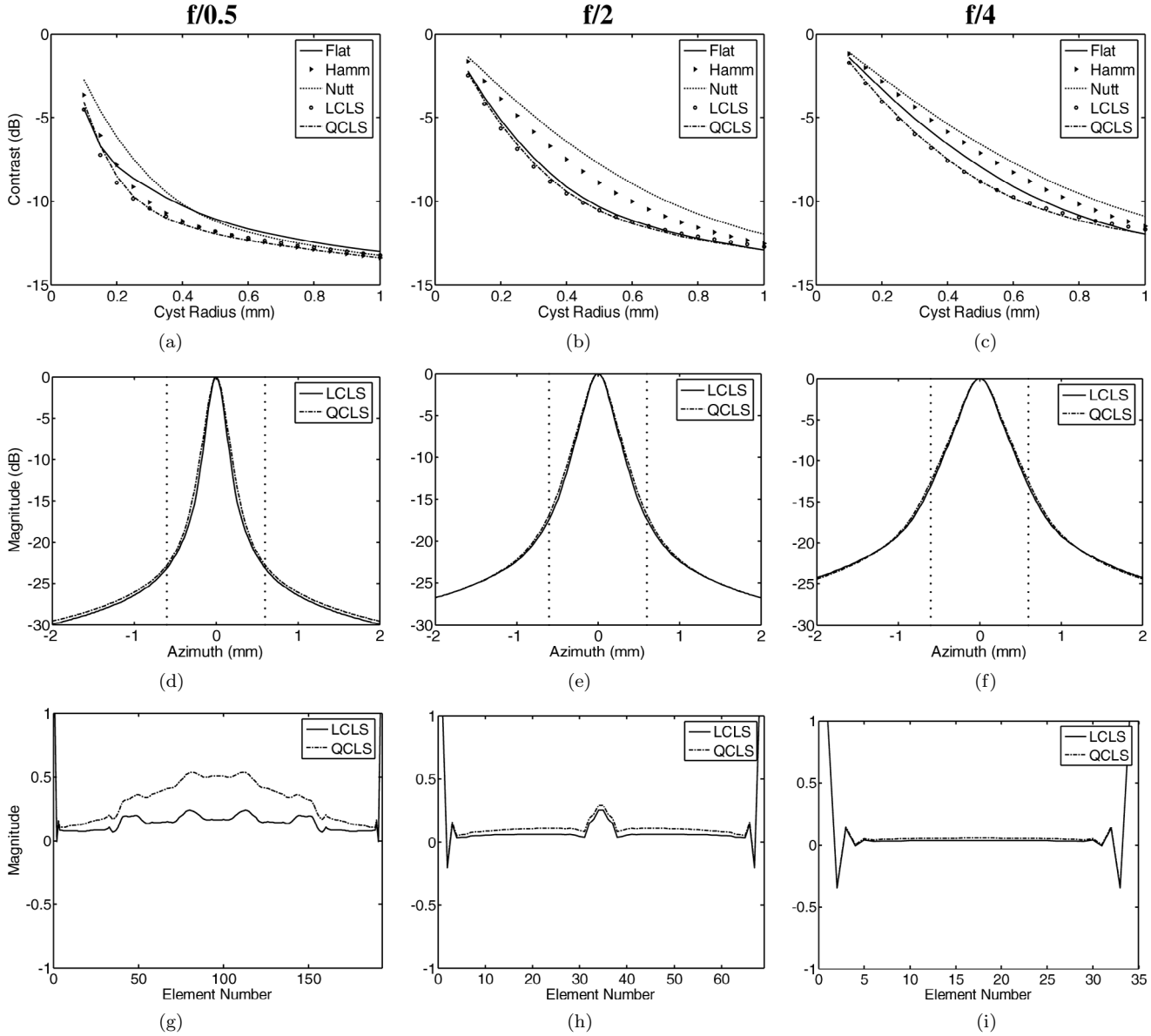

Fig. 9. Comparison of apodization profiles at different f/#'s on receive (f/0.5, f/2, and f/4). These simulations use the 10 MHz linear array with fixed transmit focus at 2 cm (f/4) and dynamic receive at 2 cm. Panels (a)–(c) show contrast curves for the different apodization schemes (flat, Hamming, Nuttall, LCLS, and QCLS). Panels (d)–(f) show the integrated beamplots of the CLS profiles in which the dotted line corresponds to the cyst boundary used to design the windows. Panels (g)–(i) show the magnitude of the CLS profiles across the aperture. The CLS algorithms produce better contrast at every cyst size than the Hamming and Nuttall windows for the f/2 and f/4 apertures.

We also investigated the effect of underestimating the sound speed by 1%, 3%, and 5%, meaning that the true propagation speed through the medium was greater than 1545 m/s. These results are shown in Fig. 12. Plots (a)–(c) in Fig. 12 show the contrast curves computed with the cyst centered on the shifted PSF. The Hamming, LCLS, and QCLS curves are similar for the 5%, 3%, and 1% underestimation. The Nuttall window again achieves the best contrast for all cyst sizes in the 5% underestimation simulation. The second row of plots in Fig. 12 shows the mainlobe region of the integrated lateral beamplots for the CLS apodized PSFs. Plots (g)–(i) in Fig. 12 show the entire lateral extent of the integrated beamplots in which differences in the grating lobes for the CLS apodized PSFs can be seen. These results closely match those from the overestimated speed of sound simulations in Fig. 11.

The design radius for the speed of sound simulations was 0.6 mm. In order to be thorough, we present results showing how the contrast curves change when we apply CLS apodizations designed over a range of cyst radii (0.4 mm–1.0 mm). We show results for two simulations, one in which the sound speed was underestimated by 1% and another in which we have grossly overestimated the sound speed by 5%.

The contrast curves for the underestimated sound speed are shown in Fig. 13. The effects of design radius for the LCLS profiles are shown in the left panel of Fig. 13. The corresponding QCLS profiles are plotted on the right. The

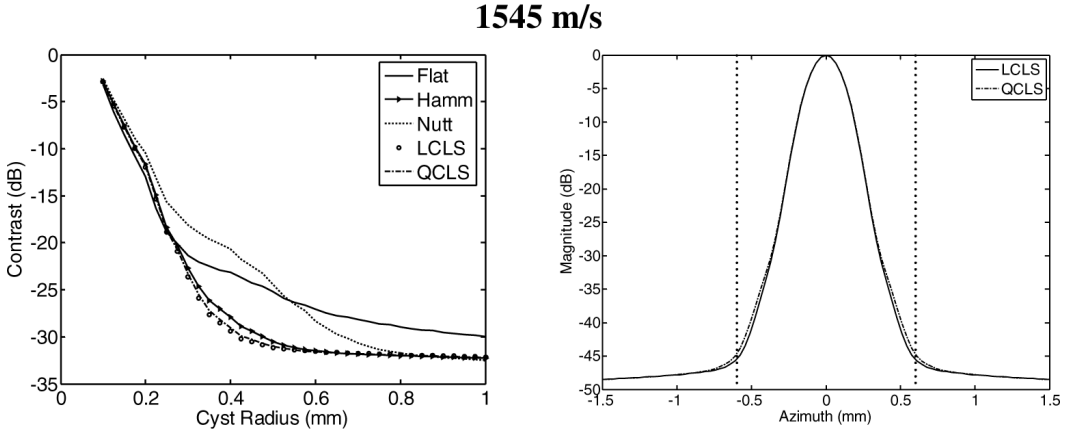

Fig. 10. Contrast curves (left) and integrated lateral beamplots (right) for the CLS apodizations designed assuming the correct speed of sound (1545 m/s). The dotted vertical lines delineate the design cyst radius of 0.6 mm. The LCLS and QCLS windows produced similar beamplots.

flat apodization contrast curve is plotted for reference in both plots. The QCLS contrast curves show more variability with design radius in which larger design radii achieve better contrast for larger cysts; but smaller design radii achieve better contrast for smaller cysts. The contrast curves corresponding to changing design radii with a 5% overestimation in speed of sound are shown in Fig. 14. The LCLS curves are shown on the left and QCLS curves are shown on the right. Both plots depict the flat apodization contrast curve for reference. In general, the curves designed with the smaller radii result in worse cystic contrast. The QCLS algorithm has a greater variability in achieved contrast than the LCLS algorithm. It should be noted that the CLS apodization profiles achieve better contrast at all cyst sizes compared with the flat apodization contrast curve.

These simulations address the concerns that the variation of sound speed in human tissues will degrade the CLS profiles. We have shown that the CLS algorithms remain relatively stable in the presence of wave propagation speed errors, but ultimately these results must be tested experimentally.

IV. Discussion

Our simulations demonstrate the use of our novel strategies for designing optimal apodization profiles. In our methods, we collect spatial impulse responses at the instant in time corresponding to the dynamic receive focus. We produce weights that minimize the energy of the spatial point spread function outside a selected radius from the mainlobe peak. This minimization is subject to a constraint that either forces unity amplitude gain at the peak of the response (LCLS method) or maintains constant energy of the PSF inside the circular region defined by the selected radius (QCLS method). The LCLS approach in general yields a narrow mainlobe and low sidelobe levels. Although such narrow mainlobes are attractive for point imaging, they may not be optimal for imaging diffuse legions and low echogenicity cysts. In these cases, the QCLS approach that yields a slightly broader mainlobe and slightly higher sidelobe levels may be desirable.

Although the LCLS and QCLS apodization design methods have been validated theoretically and through computer simulations, we must begin to assess their performance experimentally. Initial results are positive and suggest that the technique is quite robust; however, full assessment with an experimental scanner will be necessary to fully prove their efficacy. We are currently designing such experiments, and collecting the entire data set of single channel receive spatial impulse responses is a challenging task. We will need to account for spatial variance of the PSF in the lateral dimension as well as in range. Once we have fully characterized the spatial impulse response of the system, we will be able to produce CLS apodization profiles for each output image pixel, make data reconstruction seamless and rapid, and assess the performance of our algorithms to produce optimal contrast.

Obviously, the CLS apodization design algorithms can be realistically used only in a conventional system by choosing a specific design radius. Although the cystic resolution metric can be used to decide which profile can achieve the best contrast for a given application (i.e., imaging a cyst with a 0.4 mm radius or achieving −15 dB contrast for cysts ranging from 0.2 mm to 2.0 mm), the definitive optimal CLS profile is difficult to determine. We have found empirically that choosing the profile around the point at which the contrast curve begins to level off results in the best contrast for the entire range of cyst sizes. Typically, the apodization profiles at the extreme ends of the design cyst radius range exhibit more erratic behavior, like the multiple mainlobe phenomenon in the QCLS case with the large design cyst radii or the large sidelobes in the minimum beamwidth LCLS case in Fig. 1. Ideally, a library of CLS profiles could be constructed and specific profiles applied, depending on the imaging application. A peripheral vasculature exam in which contrast for larger voids would be important might use a profile designed for larger cysts while breast imaging, in which finer detail is critical might use a profile designed for a smaller cyst.

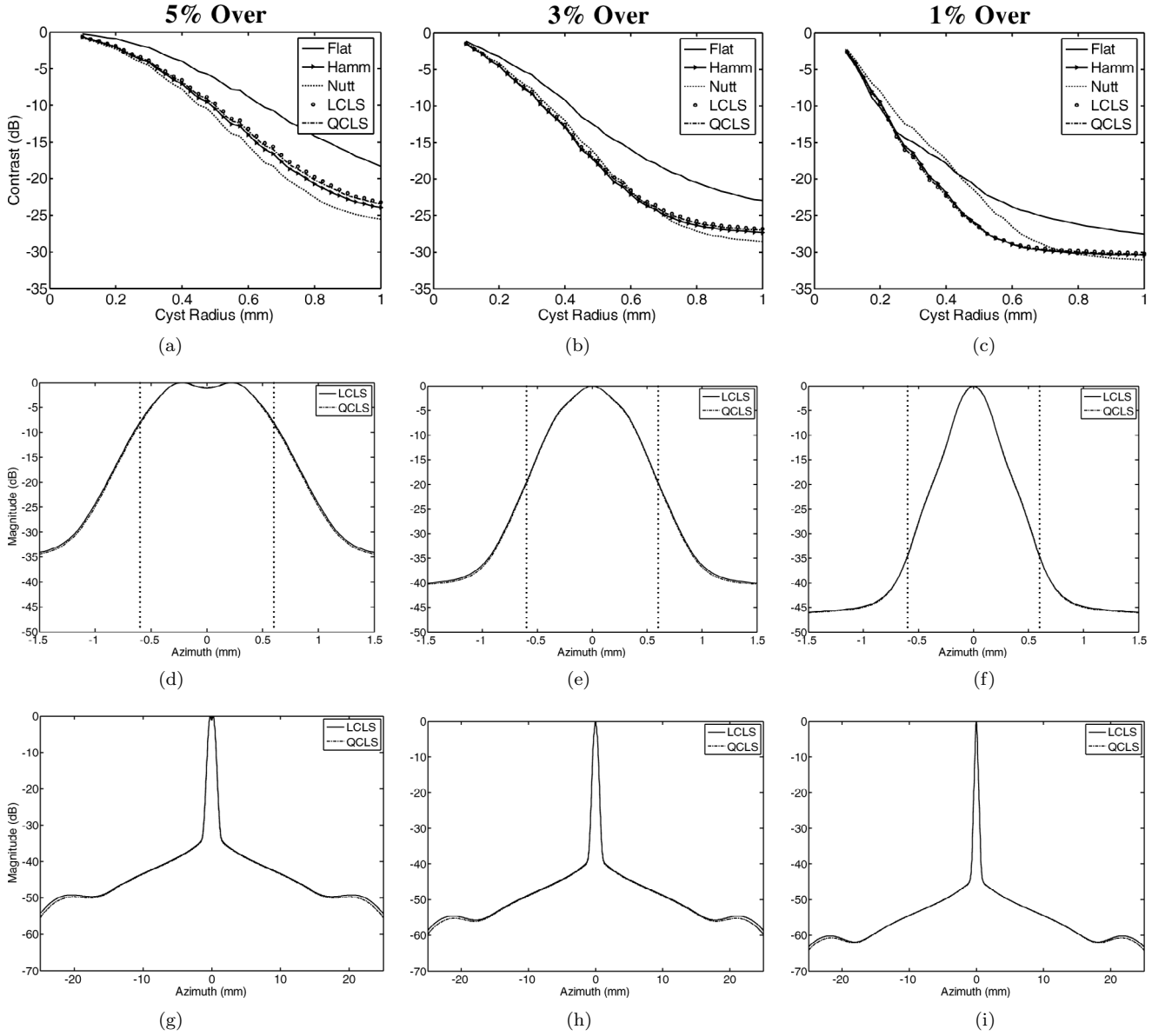

Fig. 11. Effect of assumed sound speed on the CLS algorithm. For these simulations, the wave propagation speed was overestimated by 1%, 3%, and 5%. The CLS profiles computed for 1545 m/s were applied to the degraded PSFs. Panels (a)–(c) show the resulting contrast curves. The Hamming, LCLS, and QCLS contrast curves are similar at the different sound speeds. Panels (d)–(f) plot the mainlobe region of the CLS apodized PSFs in which the dotted line delineates the design radius of 0.6 mm. The entire lateral extent of the integrated beamplots for the CLS apodized PSFs are shown in (g)–(i). The CLS algorithms remain quite stable for the sound speed errors investigated, in which the worst cystic contrast is for the simulation corresponding to the grossest sound speed error of 5%. It is interesting to note that the Nuttall window, which performs the worst at the correct speed of sound (Fig. 10), outperforms all other windows for the 5% overestimation simulation.

It is important to note that our contrast analysis is for a specific instant in time, when the PSF is centered directly in the middle of the cyst. For the speed of sound simulations in which errors in the assumed wave propagation speed shift the PSF in range, we still calculate contrast with the PSF centered on the cyst. Furthermore, the contrast resolution metric describes the point contrast of an image, not the overall contrast of the cyst. Overall cystic contrast analysis requires taking a B-mode image of a cyst, integrating the intensities over the lesion, and comparing this to the integrated intensity over a region of background speckle of the same size at the same depth [19], [20]. Extending the contrast resolution metric to incorporate overall cystic contrast is an area of ongoing research.

Results presented in this paper show that the CLS algorithms for apodization design outperform conventional windows such as the Hamming, Nuttall, and flat apodizations across a range of imaging scenarios and system parameters. The contrast curve results must be interpreted with caution because the resolution metric used to compute the cystic contrast is a point contrast value not the contrast of the overall anechoic region compared to the background speckle. We intend to perform human observer studies that will further investigate the use of the CLS

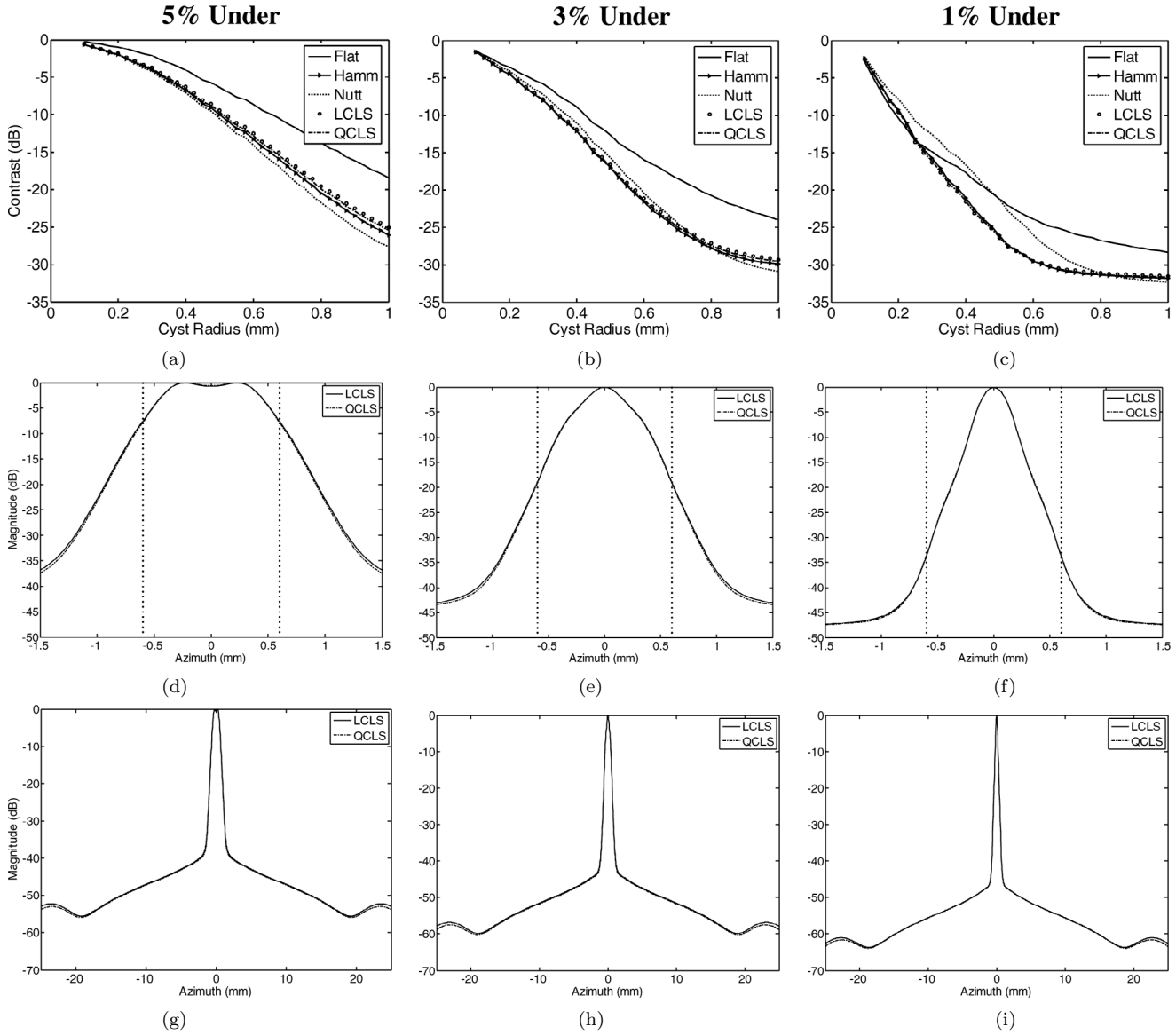

Fig. 12. Effect of assumed sound speed on the CLS algorithm. For these simulations, the wave propagation speed was underestimated by 1%, 3%, and 5%. The CLS profiles computed for 1545 m/s were applied to the degraded PSFs. Panels (a)–(c) show the resulting contrast curves. The Hamming, LCLS, and QCLS contrast curves are similar at the different sound speeds. Panels (d)–(f) show the mainlobe region of the CLS apodized PSFs in which the dotted line delineates the design radius of 0.6 mm. The entire lateral extent of the integrated beamplots for the CLS apodized PSFs is shown in (g)–(i). The CLS algorithms remain quite stable for the sound speed errors investigated. These results closely resemble those seen for the overestimated sound speeds in Fig. 11.

apodization profiles for optimal cystic contrast and, based on the simulation results presented, we believe that the CLS windows will meet our expectations. Overall the CLS apodization design technique has the potential to improve contrast of anechoic legions but also improve beamforming in general due to the formation of PSFs that have narrower mainlobes and lower sidelobes than the conventional windows. There also exists the potential for the technique to aid in the design of system responses used for hyperthermia applications and Doppler signal processing. In order for our technique to be implemented on a clinical system, adequate characterization of the system is required, including the shift variance of the PSF. However, once the system has been characterized, our algorithms save a great deal of time by obviating iterative design.

V. Conclusions

The CLS array pattern synthesis technique presented in this paper has been shown to be effective in designing apodization profiles that can improve contrast in ultrasound images. The LCLS approach achieved a 2-D spatial impulse response with a narrower mainlobe and lower sidelobes than conventional windows currently used to reduce clutter. In cases in which imaging cysts or anechoic regions are of importance and a wider mainlobe may improve cystic resolution, the QCLS technique can be used for improved contrast. We have shown that our algorithms are stable across imaging scenarios such as dynamic receive focusing, varying f/#, and different transmit frequencies. The LCLS and QCLS algorithms also improved DOF

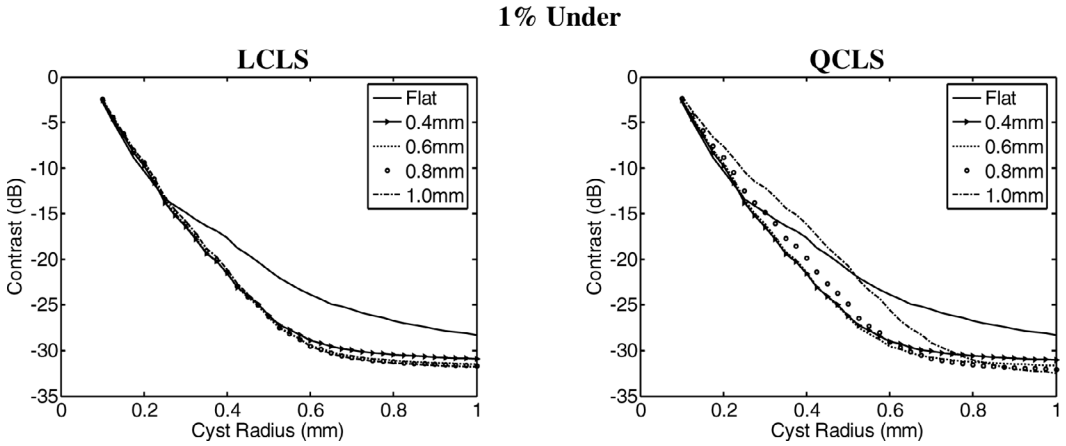

Fig. 13. Effect of design cyst radius when the assumed sound speed has been underestimated by 1%. The LCLS (left) and QCLS (right) apodization profiles were designed for 0.4 mm, 0.6 mm, 0.8 mm, and 1.0 mm cyst radii. The flat apodization contrast curve is shown for reference. The CLS profiles achieve better contrast than flat apodization across a wide range of cyst sizes. The LCLS and QCLS contrast curves remain stable in the presence of sound speed errors. The QCLS curves in general decrease contrast for the smaller cyst sizes as the design cyst radius increases.

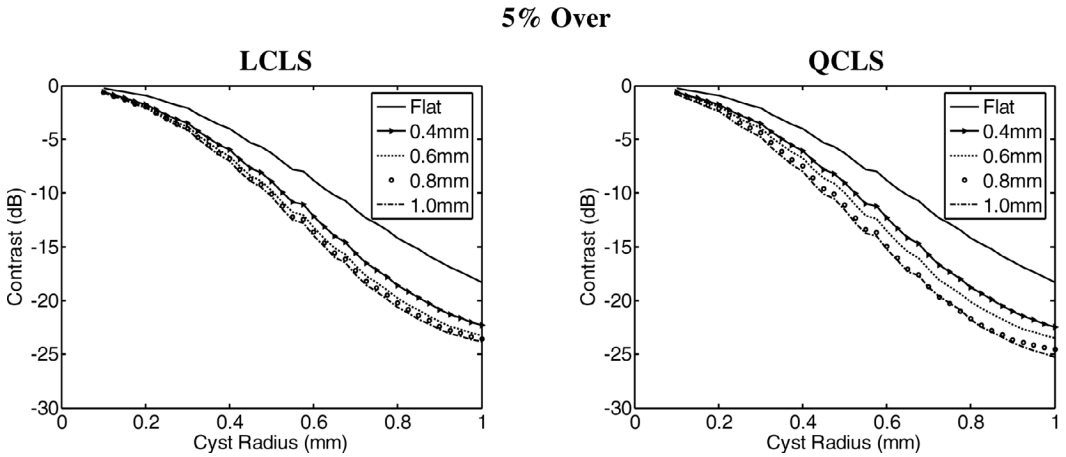

Fig. 14. Effect of design cyst radius when the assumed sound speed has been grossly overestimated by 5%. The LCLS (left) and QCLS (right) apodization profiles were designed for 0.4 mm, 0.6 mm, 0.8 mm, and 1.0 mm cyst radii. The flat apodization contrast curve is shown for reference. The LCLS and QCLS contrast curves produce better contrast than the flat apodization at all cyst sizes. In general, contrast improves for larger design cyst radii.

by maintaining relatively constant beamwidths through range. In cases in which the wave propagation speed is different than the assumed sound speed, the algorithms remain stable and still can improve contrast. Simulation results obtained by implementing the CLS algorithms demonstrate the success of the technique in solving common problems associated with ultrasound imaging, such as a restricted depth of field.

The CLS apodization design algorithms have significant potential to improve ultrasound beamforming and can be applied in any ultrasound application in which the system response is well characterized. There is no iteration involved in producing the apodization profiles; therefore, design time is considerably reduced as compared to other optimal apodization design techniques. Further investigation is required to examine the effects of phase aberration, blocked elements, shift variance of the system response, and overall cystic contrast. However, our simulations indicate that the CLS techniques improve cystic resolution and consistently outperform current conventional apodization profiles.

References

[1] D. A. Guenther and W. F. Walker, "Optimal apodization design for medical ultrasound using constrained least squares. Part I: Theory," *IEEE Trans. Ultrason., Ferroelect., Freq. Contr.*, vol. 54, no. 2, pp. 332–342, 2007.

[2] J. W. Goodman, *Introduction to Fourier Optics*. 3rd ed. Englewood, CO: Roberts, 2005.

[3] A. R. Selfridge, G. S. Kino, and B. T. Khuri-Yakub, "A theory for the radiation pattern of a narrow-strip acoustic transducer," *Appl. Phys. Lett.*, vol. 37, no. 1, pp. 35–36, 1980.

[4] L. L. Scharf, *Statistical Signal Processing: Detection, Estimation, and Time Series Analysis*. Reading, MA: Addison-Wesley, 1991.

[5] S. Docolo and M. Moonen, "Design of far-field and near-field broadband beamformers using eigenfilters," *Signal Process.*, vol. 83, pp. 2641–2673, 2003.
[6] W. H. Gander, "Least squares with a quadratic constraint," *Numerische Mathematik*, vol. 36, pp. 291–307, 1981.
[7] M. Ellis, D. A. Guenther, and W. F. Walker, "A spline based approach for computing spatial impulse responses," *IEEE Trans. Ultrason., Ferroelect., Freq. Contr.*, submitted for publication.
[8] K. Ranganathan and W. F. Walker, "A general cystic resolution metric for medical ultrasound," *IEEE Trans. Ultrason., Ferroelect., Freq. Contr.*, submitted for publication.
[9] M. E. Anderson, "The impact of sound speed errors on medical ultrasound imaging," *J. Acoust. Soc. Amer.*, vol. 107, no. 6, pp. 3540–3548, 1997.
[10] J. T. Bushberg, J. A. Seibert, E. M. Leidholt, Jr., and J. M. Boone, *The Essential Physics of Medical Imaging*. 2nd ed. New York: Lippincott, Williams, and Wilkins, 2002.
[11] W. F. Walker and G. E. Trahey, "The application of k-space in pulse echo ultrasound," *IEEE Trans. Ultrason., Ferroelect., Freq. Contr.*, vol. 45, pp. 541–558, 1998.
[12] Y.-M. Law and C.-W. Kok, "Constrained eigenfilter design without specified transition bands," *IEEE Trans. Circuits Syst. II*, vol. 52, no. 1, pp. 14–21, 2005.
[13] S.-C. Pei and J.-J. Shyu, "2-D FIR eigenfilters: A least-squares approach," *IEEE Trans. Circuits Syst.*, vol. 37, no. 1, pp. 24–43, 1990.
[14] J. A. Jensen and P. Munk, "A new method for estimation of velocity vectors," *IEEE Trans. Ultrason., Ferroelect., Freq. Contr.*, vol. 45, pp. 837–851, 1998.
[15] M. E. Anderson, "Spatial quadrature: A novel technique for multidimensional velocity estimation," in *Proc. IEEE Ultrason. Symp.*, 1997, pp. 1233–1238.
[16] W. F. Walker and G. E. Trahey, "A fundamental limit on delay estimation using partially correlated speckle signals," *IEEE Trans. Ultrason., Ferroelect., Freq. Contr.*, vol. 42, pp. 301–308, 1995.
[17] E. S. Ebbini and C. Cain, "Multiple-focus ultrasound phased-array pattern synthesis: Optimal driving-signal distributions for hyperthermia," *IEEE Trans. Ultrason., Ferroelect., Freq. Contr.*, vol. 36, no. 5, pp. 540–548, 1989.
[18] I. W. Selesnick, M. Lang, and C. S. Burrus, "Constrained least square design of FIR filters without specified transition bands," *IEEE Trans. Signal Processing*, vol. 44, no. 8, pp. 1879–1892, 1996.
[19] S. W. Smith, R. F. Wagner, J. M. Sandrik, and H. Lopez, "Low contrast detectability and contrast/detail analysis in medical ultrasound," *IEEE Trans. Sonics Ultrason.*, vol. 30, no. 3, pp. 164–173, 1983.
[20] S. W. Smith and H. Lopez, "A contrast-detail analysis of diagnostic ultrasound imaging," *Med. Phys.*, vol. 9, no. 1, pp. 4–12, 1982.
[21] A. H. Nuttall, "Some windows with very good sidelobe behavior," *IEEE Trans. Acoust. Speech Signal Processing*, vol. 29, no. 1, pp. 84–91, 1981.

Drake A. Guenther received his B.S.E. degree in biomedical engineering in 2003 from Duke University, Durham, NC. His undergraduate research as a Pratt Fellow explored adaptive beamforming and spatial compounding in ultrasound.

After completing his B.S.E., he joined the Department of Biomedical Engineering at the University of Virginia, Charlottesville, VA, where he is currently pursuing his Ph.D. degree. His research interests include ultrasound beamforming, signal processing, and angular scatter imaging.

William F. Walker (S'95–M'96) received the B.S.E. and Ph.D. degrees in 1990 and 1995 from Duke University, Durham, NC. His dissertation explored fundamental limits on the accuracy of adaptive ultrasound imaging.

After completing his doctoral work, he stayed at Duke as an assistant research professor in the Department of Biomedical Engineering. At the same time, he served as a Senior Scientist and President of NovaSon Corporation located in Durham, NC. In 1997 he joined the faculty of the Department of Biomedical Engineering at the University of Virginia, Charlottesville, VA, being promoted to associate professor in 2003. He is an active founder in two ultrasound-based startup companies, PocketSonics Inc., Charlottesville, VA, and HemoSonics LLC, Charlottesville, VA.

His research interests include aperture domain processing, beamforming, angular scatter imaging, tissue elasticity imaging, low-cost system architectures, and time-delay and motion estimation.